Supplementary Information (SI) for EES Catalysis.
This journal is © The Royal Society of Chemistry 2025

Electronic Supplementary Information

Understanding CO_2 Reduction Selectivity in Silver and Gold Electrocatalysts Using Atomically Precise Nanoclusters

Hoeun Seong,[‡a] Fang Sun,[‡b] Qing Tang,*[b] and Dongil Lee*[a]

[a]Department of Chemistry, Yonsei University, Seoul 03722, Republic of Korea

[b]School of Chemistry and Chemical Engineering, Chongqing Key Laboratory of Theoretical and Computational Chemistry, Chongqing University, Chongqing 401331, China

[‡]H.S. and F.S. contributed equally to this work.

*Corresponding Authors E-mails:

qingtang@cqu.edu.cn (Q.T.); dongil@yonsei.ac.kr (D.L.)

Methods

NC Catalyst and Electrode Preparation. All the chemicals were used as received without additional purification.

$Ag_{25}(SPhMe_2)_{18}^-$ nanocluster (NC) (referred to as Ag_{25}), where $SPhMe_2$ represents 2,4-dimethylbenzenethiolate, was synthesized using a one-phase procedure.[1] Initially, silver nitrate (Alfa Aesar, 99.9%, 0.040 g) was dissolved in 2.0 mL of water, followed by the addition of tetrahydrofuran (16 mL) to the vigorously stirred solution. Subsequently, 2,4-dimethylbenzenethiol (TCI, 96%, 0.090 mL) was introduced into the solution. Tetraphenylphosphonium bromide (Merck, 97%, 6 mg) in 0.5 mL of methanol and sodium borohydride (Merck, 99%, 15 mg) in 0.5 mL of water were then sequentially added to the reaction mixture, which was allowed to react for 30 min. The solvent was evaporated, and the crude product was collected using dichloromethane (4.0 mL), with large-sized impurities being precipitated by the addition of methanol (8.0 mL). Finally, the Ag_{25} NC was obtained through centrifugation after the addition of 16.0 mL of methanol and purified by washing with a copious amount of methanol.

$Au_{25}(SEtPh)_{18}^-$ NC (Au_{25} for short), where SEtPh is 2-phenylethanethiolate, was synthesized using a one-phase method.[2] $HAuCl_4 \cdot 3H_2O$ (Merck, reagent grade, 0.197 g) and tetraoctylammonium bromide (Merck, 98%, 0.317 g) were dissolved in tetrahydrofuran (15 mL) and stirred for 5 min. Subsequently, 2-phenylethanethiol (Merck, 98%, 0.360 mL) was added to the solution. After stirring for 1 h, a solution of sodium borohydride (0.190 g) in water (5 mL) was added, and the reaction was allowed to proceed for 24 h. Separating organic phase solution, the Au_{25} NC was then collected by centrifugation after adding methanol (14.0 mL) to the organic solution.

Gas diffusion electrodes (GDEs) with a microporous layer (MPL) (Ce-Tech, W1S1011) served as the substrate for immobilizing catalysts. GDEs coated with Ag (Merck, <100 nm particle size, 99.5%) and Au (Merck, <100 nm particle size, 99.9%) nanoparticles (NPs) (referred to as AgNP/GDE and AuNP/GDE, respectively) were fabricated through drop-casting a dispersion of 6.25 mg of NPs and 0.06 mL of Nafion (Merck, 5 wt%) in isopropyl alcohol (0.5 mL) onto the GDE (6.25 cm^2). The loading of the NPs was 1.0 mg cm^{-2}.

GDEs coated with Ag_{25} and Au_{25} NCs (Ag_{25}/GDE and Au_{25}/GDE, respectively) were prepared by drop-casting the catalyst ink, in which 66 nmol of NCs are dissolved in a mixed solvent of acetone (0.16 mL) and dichloromethane (0.16 mL). The drop-casting was done onto the MPL side of the GDE (6.25 cm^2). The typical loading of the NCs was 10.6 nmol cm^{-2} (0.06 mg cm^{-2} for Ag_{25} and 0.08 mg cm^{-2} for Au_{25}).

NC Catalyst Characterization. Ultraviolet–visible (UV–vis) absorption spectra of the NC dichloromethane solutions were obtained using a UV–vis–NIR spectrophotometer (Shimadzu, UV-3600). Electrospray ionization (ESI) mass spectra were acquired with a mass spectrometer (Agilent, 6230 TOF LC/MS) by directly injecting NC dichloromethane solutions (0.1 mg mL^{-1}). X-ray photoelectron spectroscopy (XPS) was conducted using a K-alpha system (Thermo, UK) with a monochromatic Al Kα X-ray source (1486.6 eV). Samples were loaded onto glass for analysis, and binding energies were calibrated against the C 1s peak at 285 eV. High-angle annular dark-field scanning transmission electron microscopy (HAADF-STEM) images were obtained with an aberration-corrected transmission electron microscope (JEOL, JEM-ARM200F NEOARM) operated at 200 kV.

NC Catalyst Activation. Electrochemically activated NCs were obtained using a previously reported method.[3] Both Ag_{25}/GDE and Au_{25}/GDE underwent activation via constant potential electrolysis at –0.96 V versus reversible hydrogen electrode (RHE) for 2 h before assessing their electrochemical characteristics. The activated NC catalysts were examined post-recovery from the electrodes. However, retrieving the NC catalysts from the GDE was challenging due to the strong hydrophobic interaction between the GDE and the organic ligands of the NCs. Thus, a nickel foam (NF, 29-04275-01, Invisible Inc.) substrate was utilized. To ensure uniform activation of all NCs on the electrode, a thin catalyst layer (2 nmol cm^{-2}) was applied on a large-area NF (100 cm^2) by dropcasting a diluted NC solution (200 nmol in 10 mL of acetone-dichloromethane). An NC-immobilized NF electrode was activated similarly to the NC/GDEs (–0.96 V versus RHE for 2 h). Following electrochemical activation, the electrode was rinsed thoroughly with copious amounts of water and methanol to eliminate residual electrolyte salts and detached ligands, respectively. Subsequently, the activated NCs were extracted using CH_2Cl_2 (30 mL). Over 90% of the activated NCs were successfully retrieved.

CO_2 Electroreduction in a Flow Electrolyzer. Electrochemical measurements and product analysis were conducted using a flow electrolyzer setup (illustrated in **Fig. S4**). A peristaltic pump (Signal, iPump 2L) delivered fresh electrolyte solution at a constant flow rate of 1.0 mL min^{-1} to the front side of both the cathode and anode. A mass flow controller (MFC Korea Co., Ltd., EPC-220) regulated the continuous flow of CO_2 or Ar gas at a rate of 20 mL min^{-1} to the rear side of the cathode. A catalyst-coated GDE and an NF electrode was used as the cathode and anode, respectively. An anion exchange membrane (FuMA-Tech, FAAM-40) separated the cathode and anode chambers. Cathodic potentials were recorded with respect to a Ag/AgCl electrode (CH Instruments, CHI111, filled with 3.0 M KCl) using a potentiostat (WonATech, ZIVE BP2). The electrochemical experiments were conducted and averaged out of 2-3 independent experiments. The electrochemical experiments were very reproducible with the precise loading control of NCs at the molecular level and the error bars were actually smaller than the symbol size in the graphs. These potentials were converted to the standard hydrogen electrode (SHE) scale by adding +0.21 V. The potentials in the SHE scale were further converted to the RHE scale by the following Nernst equation, and to the overpotential:

$$E \text{ (versus RHE)} = E \text{ (versus SHE)} + 0.059 \times \text{pH} \quad \text{(S1)}$$

$$\text{Overpotential} = \left| E \text{ (versus RHE)} + 0.11 \text{ V} \right| \quad \text{(S2)}$$

After 3 minutes the potential applied, the outlet gas was analyzed using gas chromatography (Agilent, GC 7890B) equipped with a thermal conductivity detector and a flame ionization detector. Only CO and H_2 were generated on the Ag and Au catalyst-coated GDEs. All electrochemical measurements were conducted

***In-situ* Electrochemical Infrared Measurements.** Operando attenuated total reflection (ATR)–Fourier-transform infrared (FTIR) measurements were performed in an ATR cell using a special accessory of a Ge horizontal ATR (HATR) crystal (Pike Technologies) with an FTIR spectrophotometer (Thermo Fisher Scientific, Nicolet iS50) equipped with a mercury cadmium telluride detector. The ATR cell was filled with a 1.0 M $NaClO_4$ electrolyte solution (30 mL) and purged with CO_2 or Ar gas for 30 min before the experiments, and the gas was continuously supplied to the solution during the experiments. The working electrode (NC/GDEs, 7 × 0.5 cm^2) was placed on the HATR crystal with the MPL side facing the crystal. A Pt foil (2 cm^2) served as the counter electrode, and a Ag/AgCl (1.0 M KCl) electrode was used as the reference electrode. The CPE measurements were conducted at –1.8 V versus SHE, and ATR FTIR spectra were recorded at 25 s time intervals. All data were corrected by subtracting the background spectra obtained at open circuit potential.

DFT Calculations. The spin-polarized density functional theory (DFT) calculations on the electrocatalytic activity were performed using Vienna ab initio simulation package (VASP5.4.4).[4] The nanoclusters were put in a cubic box (25 Å × 25Å × 25 Å), and their structures were optimized by the Perdew-Burke-Ernzerhof (PBE) function form of the generalized gradient approximation (GGA) to represent the interactions of electron exchange-correlation.[5] The projector-augmented-wave (PAW) method was carried out to describe the ion-electron interactions,[6] and the wave functions of all the computations were expanded via a plane-wave cutoff energy of 400 eV. The convergence criteria for energy and force were set as 10^{-5} eV and 0.02 eV A^{-1} for maximal displacement, respectively. The Brillouin zone was sampled through the Γ point for geometry optimization. In addition, we utilized the empirical density functional dispersion (DFT–D3) method[7] to consider the van der Waals interactions between ligands. All atoms were unconstraint and fully relaxed during the simulation.

Based on the computational hydrogen electrode (CHE) model,[8] the change of Gibbs free energy (ΔG) for each CO_2RR elementary reaction can be calculated as:

$$\Delta G = \Delta E + \Delta E_{sol} + \Delta ZPE - T\Delta S \quad \text{(S3)}$$

where ΔE, ΔZPE and ΔS are the change of the total energy that can be directly obtained from DFT calculations, the difference of zero-point energy, and the change of entropy at 298.15 K, respectively. The ΔE_{sol} represents a

solvation correction. For *COOH and *CO, the solvation correction is –0.25 eV and –0.1 eV, respectively.[9] For the adsorbed intermediates, only vibrational entropy is considered, which is calculated from the DFT calculated vibrational frequencies. In addition, due to the inaccurate description of CO_2 and CO molecules by PBE functional,[5, 10] we added correction of –0.34 eV for CO and +0.10 eV for CO_2. For the gas molecules, the entropy is taken from NIST database. The zero-point energy (ZPE) and entropy correction (–T**S*) at 298.15 K for various gas-phase species are provided in the following table.

Species	ZPE (eV)	–T**S* (eV)
CO_2	0.31	-0.66
CO	0.13	-0.61
H_2	0.27	-0.40
H_2O	0.59	-0.58

All calculations in this study were conducted using the electrically neutral supercell model. The $*CO_2^-$ intermediate referred to in the text indicates that an electron is gained from the metal surface, forming an adsorbed CO_2 species with the characteristics of an anion radical. Its electron density is mainly localized in the CO_2 unit and exhibits corresponding geometric structure variation features.

Supplementary Figures and Table

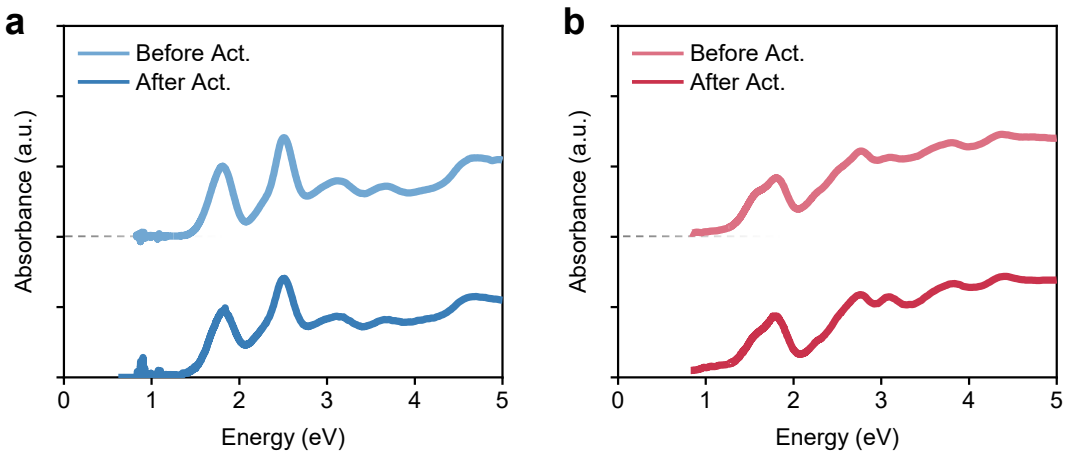

Fig. S1 UV–vis absorption spectra of CH_2Cl_2 solutions of the (a) Ag_{25} and (b) Au_{25} NCs before and after electrochemical activation.

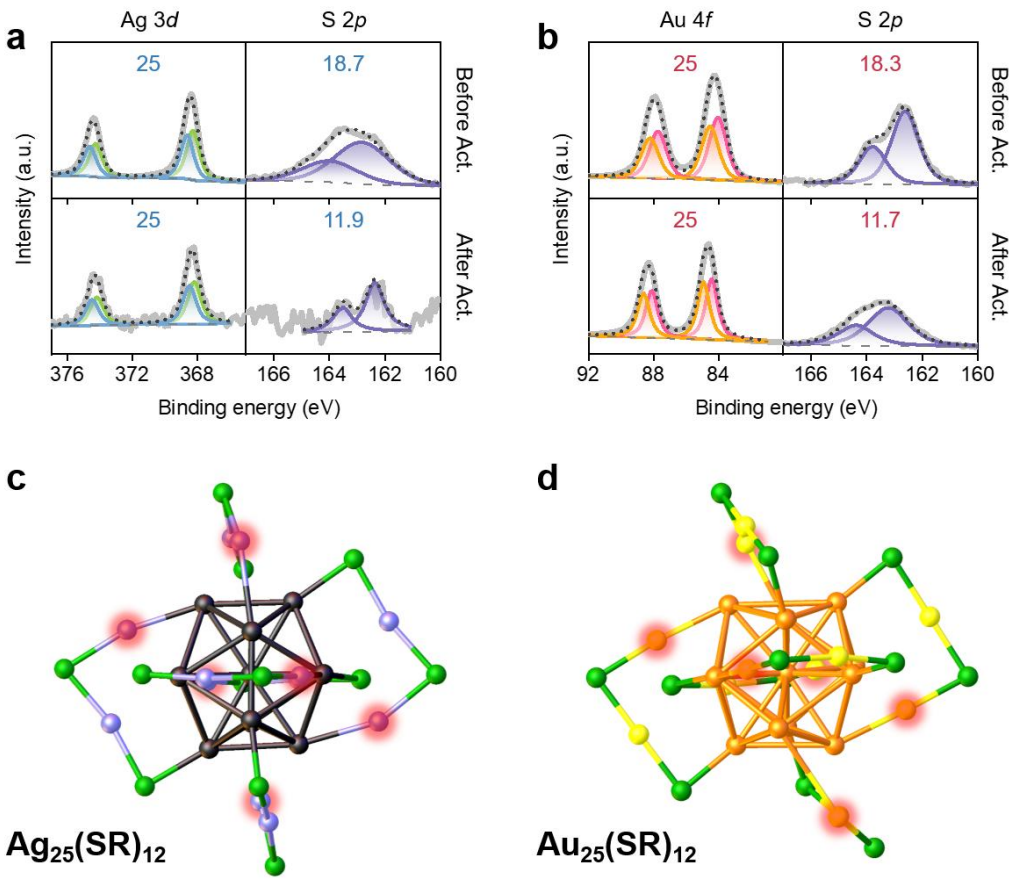

Fig. S2 XPS profiles of (a) Ag_{25} and (b) Au_{25} NCs before (above) and after (below) electrochemical activation. Experimental data (gray lines) are depicted with fitting envelopes (black dots) and component fitting lines of Ag^0 3*d* (blue), Ag^+ 3*d* (green), Au^0 4*f* (pink), Au^+ 4*f* (yellow), and S $2p_{1/2}$ and S $2p_{3/2}$ (violet). The atomic ratios are indicated in the graph. The XPS results clearly show that approximately one thiolate ligand was removed from each staple of the M_{25} NCs. DFT-optimized atomic structures of (c) $Ag_{25}(SR)_{12}$ and (d) $Au_{25}(SR)_{12}$ NCs after ligand removal. Dethiolated metal sites are highlighted in red. Alkyl chains of the thiolate ligands are omitted for clarity.

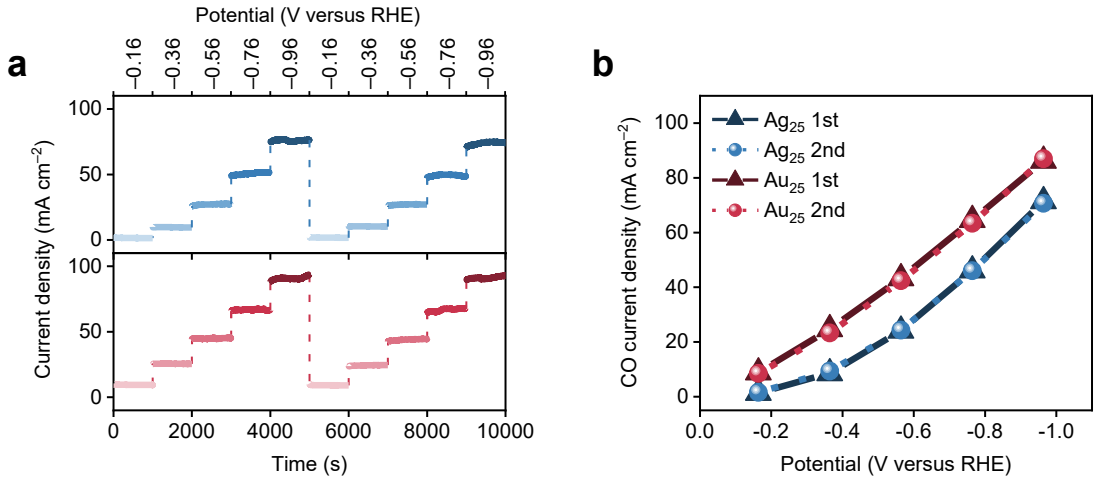

Fig. S3 (a) Staircase voltammograms of Ag_{25}/GDE and Au_{25}/GDE, and (b) the corresponding CO current densities. The CO_2RR activities of Ag_{25}/GDE and Au_{25}/GDE remained constant at all fixed cathodic potentials during repetitive measurements. These findings strongly indicate that the immobilized NCs were consistently retained on the electrodes, enabling the monitoring of electrocatalytic reactions on the well-defined NC surfaces.

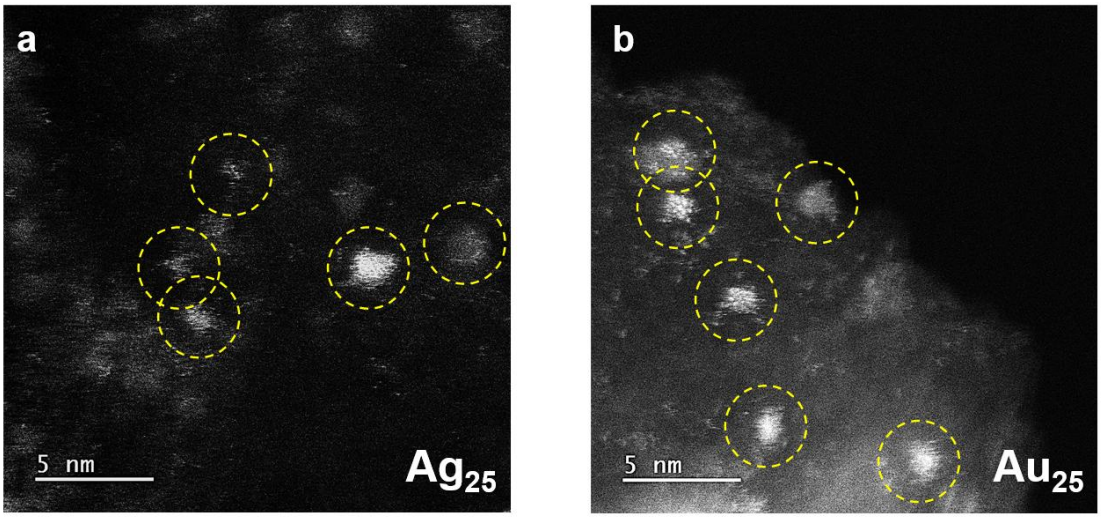

Fig. S4 Abberration-corrected HAADF-STEM images of (a) Ag_{25}/GDE and (b) Au_{25}/GDE after repetitive CPE experiments, as shown in Fig. S3.

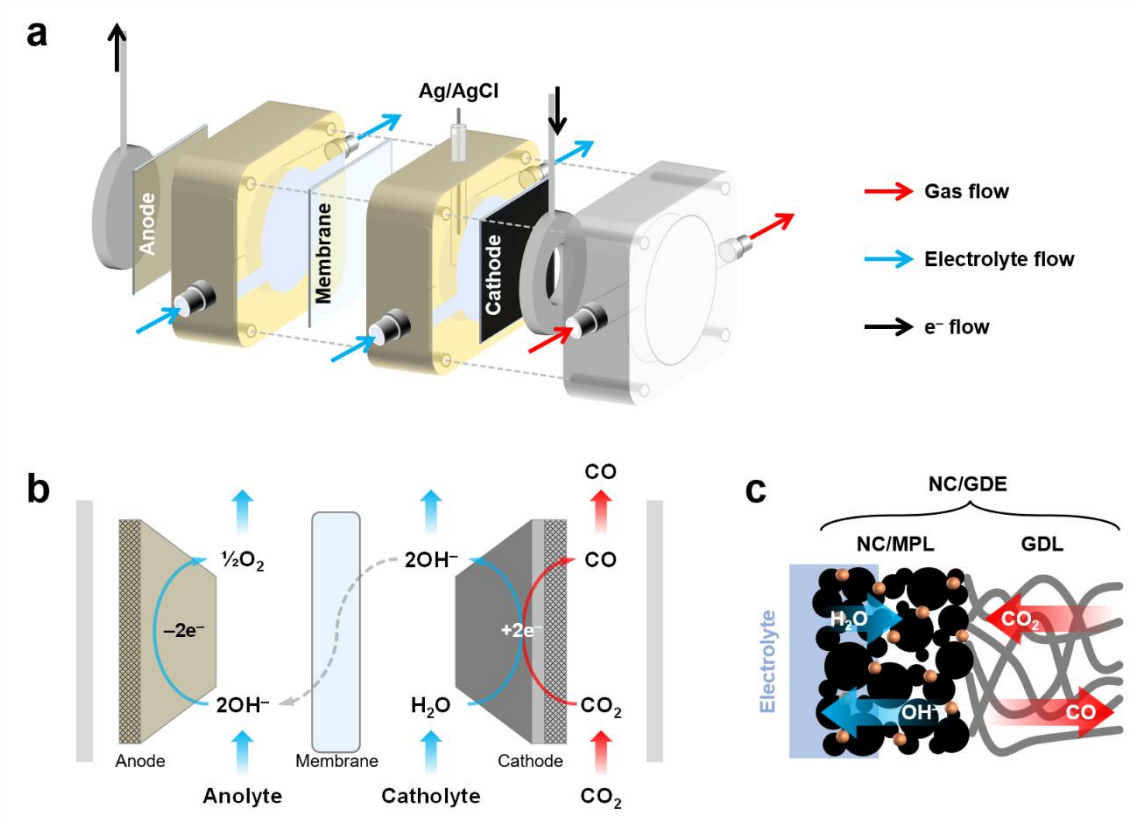

Fig. S5 Schematics of (a) the flow cell setup, (b) the flow of reactants and products, and (c) the GDE interface. Electrolyte solutions are delivered to the front side of the anode and cathode (MPL side of GDE), while a gaseous stream is directed to the back side of the cathode (GDL side of GDE). The gaseous reactant (CO_2) can be easily supplied to the catalysts' vicinity by establishing a three-phase boundary.

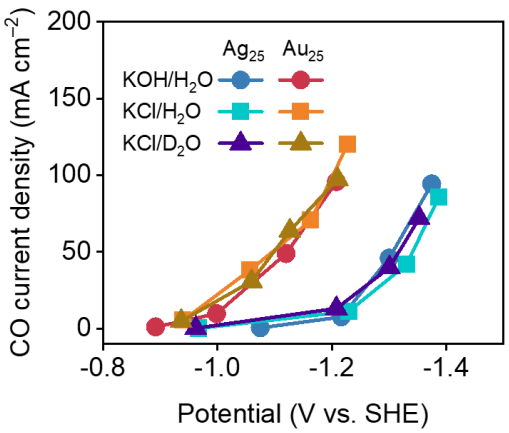

Fig. S6 CO current densities recorded on Ag_{25}/GDE and Au_{25}/GDE in a CO_2-fed flow electrolyzer at different cathodic potentials while utilizing various electrolyte solutions (concentration = 1.0 M). The data represent averages from 2–3 independent experiments, and the error bars were smaller than the symbol size in the graphs.

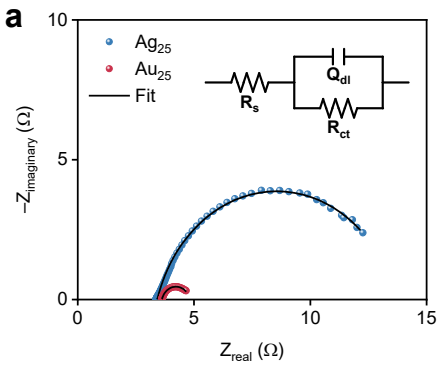

b

Catalyst	R_s (Ω)	R_{ct} (Ω)	Q_{dl} (F)	k_{et} (cm/s)
Ag_{25}	3.42	10.3	0.868	9.8
Au_{25}	3.62	1.20	0.862	84

Fig. S7 (a) Nyquist plots obtained by measuring EIS on Ag_{25}/GDE and Au_{25}/GDE during CO_2RR at –0.36 V with fitting lines. The equivalent electric circuit used to obtain the impedance parameters is shown in the inset of panel (a) (R_s: solution resistance, R_{ct}: charge-transfer resistance, Q_{dl}: constant phase element representing double layer capacitatnce). (b) Impedance parameters and electron-transfer constants (k_{et}) of the Ag_{25} and Au_{25} NCs obtained by fitting of the Nyquist plots in panel (a). The k_{et} was determined by following equation:[11] $k_{et}=RT/n^2F^2AR_{CT}C_0$, where n=2, A=2 cm^2, C_0=33 mM, and the other symbols are as commonly known.

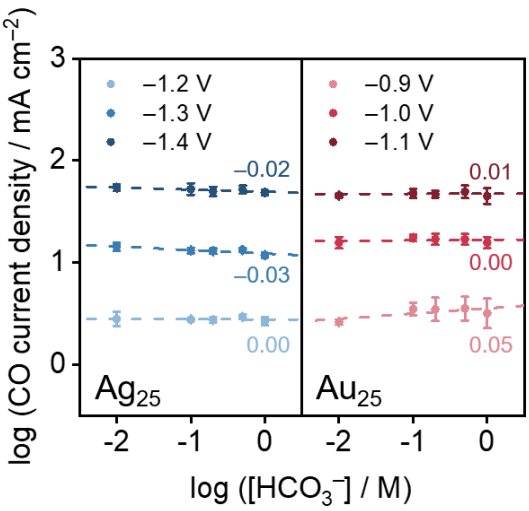

Fig. S8 Reaction order in HCO_3^- for the CO_2RR determined on the Ag_{25} and Au_{25} NCs. The graph displays the respective reaction orders. The potentials were iR-corrected.

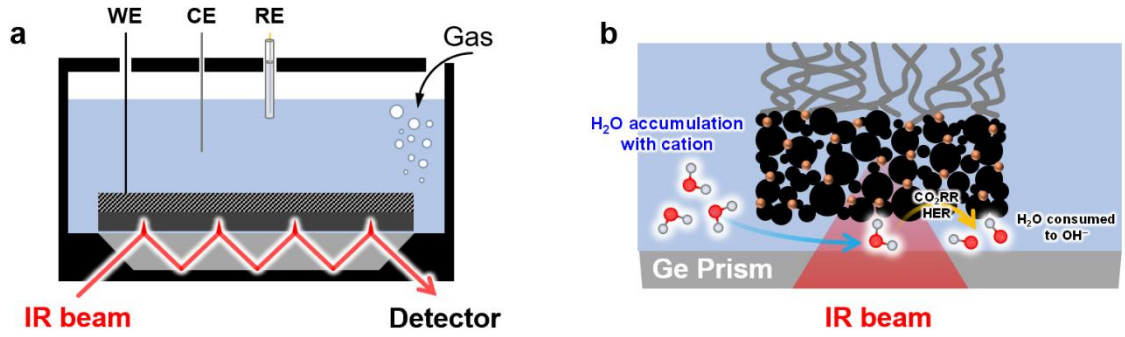

Fig. S9 Schematic of (a) an electrochemical cell for *in-situ* ATR FTIR experiments and (b) a magnified schematic illustrating the interface between the NC/GDE and the prism. It is noteworthy that the figure is not drawn to scale; the electrolyte layer between the NC/GDE and the prism is significantly thinner than the detected thickness of the NC/GDE. This thin layer enables the monitoring of water content within the NC/GDE during the CO_2RR (or the HER).

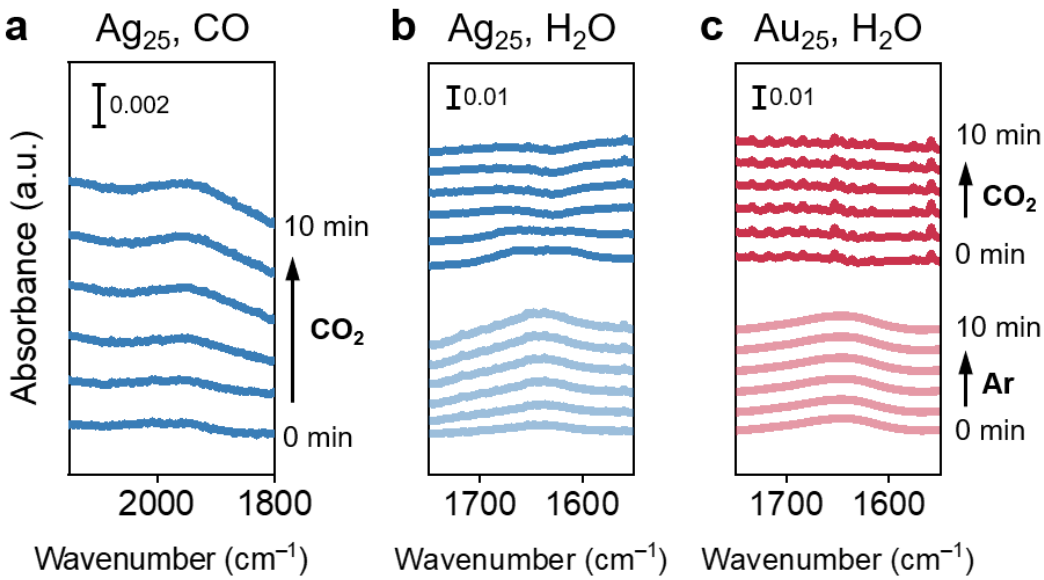

Fig. S10 Magnified ATR–FTIR spectra, emphasizing (a) the CO stretching mode of Ag_{25} and the H_2O bending modes of (b) Ag_{25} and (c) Au_{25} NCs.

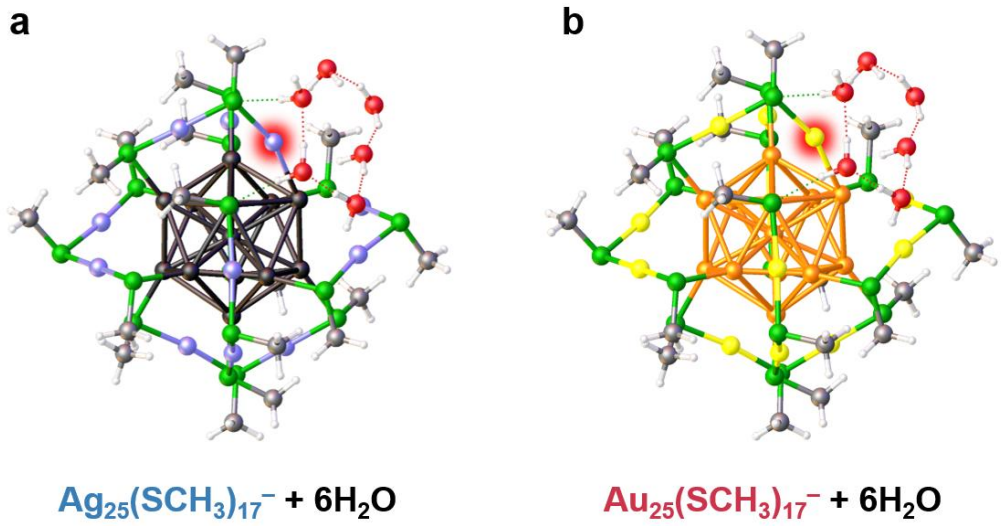

Fig. S11 Optimized structures of (a) $Ag_{25}(SCH_3)_{17}^{-}$ and $Au_{25}(SCH_3)_{17}^{-}$ NCs with six explicit water solvent molecules. By considering the redox potentials of the Ag_{25} and Au_{25} NCs,[12, 13] it is evident that the anionic NCs prevail as the primary species under the applied potentials for the CO_2RR. The dethiolated metal sites are highlighted in red.

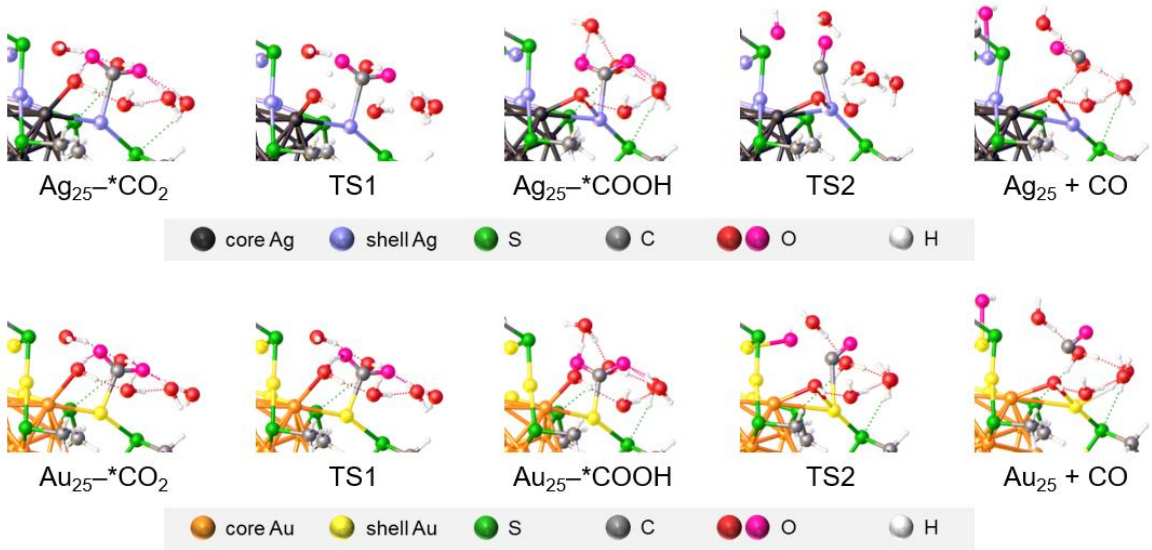

Fig. S12 The key atomic configurations for the CO_2RR on $Au_{25}(SCH_3)_{17}^{-}$ and $Ag_{25}(SCH_3)_{17}^{-}$ NCs.

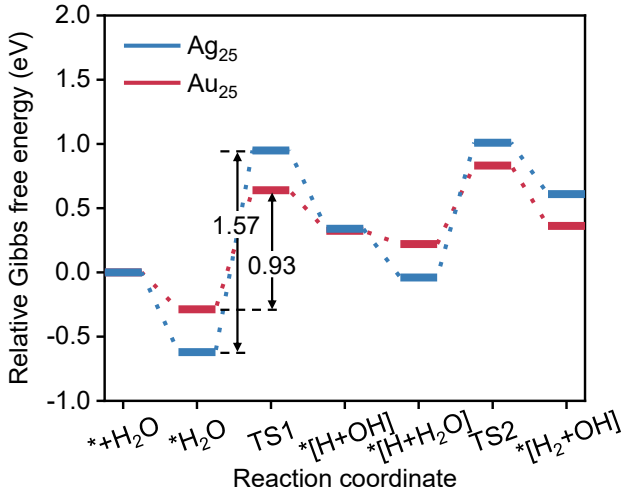

Fig. S13 (a) Free energy diagrams illustrating $2H_2O$-to-H_2 reduction intermediates on $Ag_{25}(SCH_3)_{17}^-$ and $Au_{25}(SCH_3)_{17}^-$ NCs. The initial WD steps (TS1) serve as the potential-determining steps on both NCs.

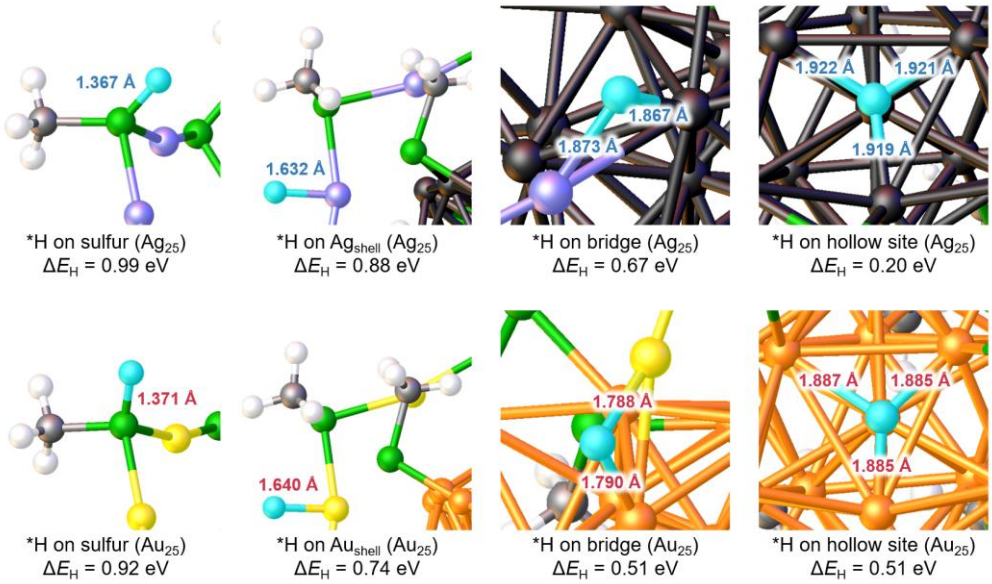

Fig. S14 The adsorption configurations and adsorption energies of hydrogen atom at different sites on $Ag_{25}(SCH_3)_{17}^-$ and $Au_{25}(SCH_3)_{17}^-$ NCs.

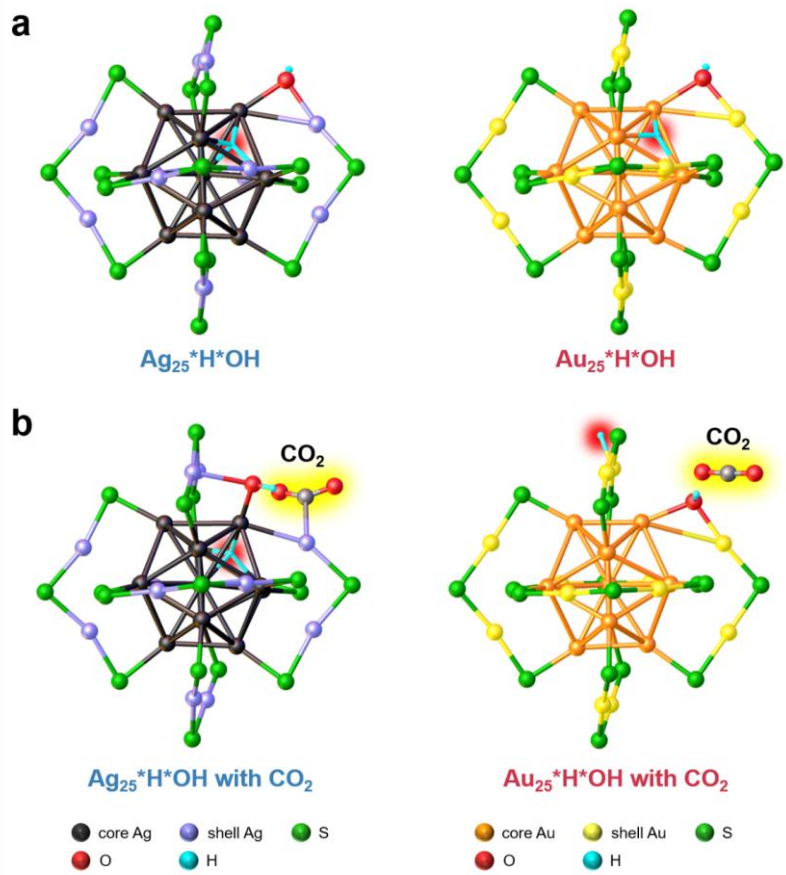

Fig. S15 Optimized intermediate structures of *H and *OH co-adsorbed on $Ag_{25}(SCH_3)_{17}^-$ and $Au_{25}(SCH_3)_{17}^-$ in the (a) absence and (b) presence of one CO_2 molecule. The adsorbed *H and the adjacent CO_2 molecule are highlighted in red and yellow, respectively.

Table S1 Atomic compositions of Ag_{25} and Au_{25} NCs before and after activation as determined through XPS.

	Before Activation		**After Activation**	
	M	**S**	**M**	**S**
Ag_{25}	**25**	**18.7**	**25**	**11.9**
Au_{25}	**25**	**18.3**	**25**	**11.7**

References

1. C. P. Joshi, M. S. Bootharaju, M. J. Alhilaly and O. M. Bakr, *J. Am. Chem. Soc.*, 2015, **137**, 11578-11581.
2. H. Seong, M. Choi, S. Park, H.-w. Kim, J. Kim, W. Kim, J. S. Yoo and D. Lee, *ACS Energy Lett.*, 2022, **7**, 4177-4184.
3. H. Seong, K. Chang, F. Sun, S. Lee, S. M. Han, Y. Kim, C. H. Choi, Q. Tang and D. Lee, *Adv. Sci.*, 2024, **11**, 2306089.
4. G. Kresse and J. Furthmüller, *Phys. Rev. B: Condens. Matter*, 1996, **54**, 11169-11186.
5. J. P. Perdew, K. Burke and M. Ernzerhof, *Phys. Rev. Lett.*, 1996, **77**, 3865-3868.
6. P. E. Blöchl, *Phys. Rev. B: Condens. Matter*, 1994, **50**, 17953-17979.
7. I. L. Garzón and A. Posada-Amarillas, *Phys. Rev. B*, 1996, **54**, 11796-11802.
8. J. K. Nørskov, J. Rossmeisl, A. Logadottir, L. Lindqvist, J. R. Kitchin, T. Bligaard and H. Jónsson, *J. Phys. Chem. B*, 2004, **108**, 17886-17892.
9. Y. Ouyang, L. Shi, X. Bai, Q. Li and J. Wang, *Chem. Sci.*, 2020, **11**, 1807-1813.
10. A. A. Peterson, F. Abild-Pedersen, F. Studt, J. Rossmeisl and J. K. Nørskov, *Energy Environ. Sci.*, 2010, **3**, 1311-1315.
11. H. Chen, P. Kannan, L. Guo, H. Chen and D.-H. Kim, *J. Mater. Chem.*, 2011, **21**, 18271-18278.
12. H. Yi, S. M. Han, S. Song, M. Kim, E. Sim and D. Lee, *Angew. Chem. Int. Ed.*, 2021, **60**, 22293-22300.
13. K. Kwak, W. Choi, Q. Tang, M. Kim, Y. Lee, D.-e. Jiang and D. Lee, *Nat. Commun.*, 2017, **8**, 14723.